INTERNATIONAL JOURNAL OF INTEGRATED ENGINEERING
ISSN: 2229-838X e-ISSN: 2600-7916

IJIE

Vol. 16 No. 7 (2024) 91-104
https://publisher.uthm.edu.my/ojs/index.php/ijie

Plasmonic Wave Validation via Finite Element Modeling and Opto-plasmonic System for Biosensor

Muhammad Rosli Abdullah[1], Noor Hasmiza Harun[1], S Noorjannah Ibrahim[2], Azimah Abdul Wahab[3], Mohd Azerulazree Jamilan[4]

[1] *Medical Engineering Technology Section, Universiti Kuala Lumpur-British Malaysian Institute, Gombak, 53100, MALAYSIA*
[2] *Department of Electrical & Computer Engineering, International Islamic University, Gombak, 53100, MALAYSIA*
[3] *Clinical & Biomedical Laboratory Science Section, Universiti Kuala Lumpur-Institute of Medical Science Technology, Kajang, 43000, MALAYSIA*
[4] *NMCRC, Institute for Medical Research, Ministry of Health Malaysia, Shah Alam, 40170, MALAYSIA*

* Corresponding Author: rosli@unikl.edu.my
DOI: https://doi.org/10.30880/ijie.2024.16.07.009

Article Info

Received: 25 June 2024
Accepted: 10 September 2024
Available online: 2 December 2024

Keywords

Plasmonic, plasmon, finite element modeling, resonance, floquet, FWHM, P-polarized

Abstract

Plasmonic is light and free electrons interaction in metal nanostructures. Free electrons are oscillated and known as plasmon when light hits the metal. Matched plasmon/ light at respective frequency/ momentum generates a resonance at maximum excitation of plasmonic energy. A resonance shift indicates significant molecular binding for biological matters. Plasmonic biosensors experience unpredictable outcomes without a theoretical agreement. finite element modeling (FEM) could investigate effects, factors and scenarios for a real-time solution. Opto-plasmonic compares FEM to optimize parameters for generating the plasmonic energy. The objective is to perform and validate FEM with an Opto-plasmonic system according to Brewster, critical and resonance angles. A 2D geometries of BK7(1000um)- Au(50nm)- Air(1000nm) were modelled in the Electromagnetic Frequency Domain with Floquet's periodic boundary condition. The Opto-plasmonic consists of 1- Optics (650nm laser, prism, slit, polarizer, photodiode), 2- Mechanical (Bipolar stepper motors, gears, stages) and 3- Electronics (PIC18F4550, LCD and drivers). The P-polarized beam was reflected via a prism and read by a photodiode at 0.045° and 0.1125°, respectively. Experimental to FEM accuracy indicates percentage differences for Θc, Θr, Δr, FWHM, and Rmin at 3.72%, 0.2%, 3.37%, 4.64% and 0%, respectively. Excellence validation was successfully achieved between FEM and Opto-plasmonic. In conclusion, the opto-plasmonic system can generate plasmonic energy for a biosensor application.

1. Introduction

Plasmonic adopt interaction between light and metal for innovative applications in nanotechnology, biomedicine, Biosensors, telecommunication, optical devices, solar power, photocatalysis, Etc. [1]–[6]. The plasmonic wave (PW) is the electromagnetic (EM) coupling under Transverse Magnetic (TM) mode with collective electron's oscillation in a conductor such as metal [7]–[9]. Referring to Fig.1, when light hits a boundary of two mediums (n1

and n2), the light will be reflected (θr) and refracted (θt). The n1 and n2 are refractive indexes of travelling and refracted rays over a different medium. As expressed by Snell's law in Equation 1, a Total Internal Reflection (TIR) in Equation 2 must exist at the interfaces when $\theta_I > \theta_C, TIR = \sin\theta_T > 1$ [10]–[12].

$$n1\ sin\ \theta_I = n2\ sin\ \theta_T \tag{1}$$

$$\sin^{-1}\left(\frac{n2}{n1}\sin\theta_T\right) > \sin^{-1}\left(\frac{n2}{n1}\right) \tag{2}$$

Therefore, TIR is when the incident light (θi) greater than 90 degrees is wholly reflected and consequently generates the evanescent wave [13]– [15]. As shown in Fig. 1(a), the wave does not propagate as an electromagnetic but instead as a confined energy, e that exponentially decays between n1 and n2 boundaries. This phenomenon can be illustrated in the Fig. 1(b) and expressed in Equation 3.

$$Re(\vec{E}_T) = \vec{E}_{0T}\cos\big((k_T\sin\theta_T)x - \omega t\big)e^{-Az} \tag{3}$$

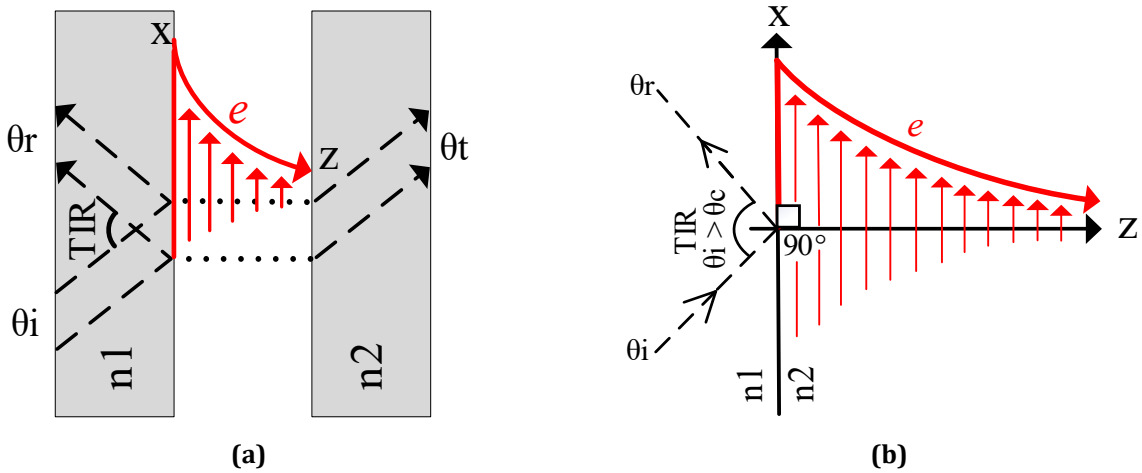

Fig. 1 *Evanescent wave*

Upon TIR, both propagation constants must fulfil the requirement of ħω (plane vector of an evanescent wave) equal to ħk (plane vector of the plasmonic wave), ħω = ħk. Referring to the Fig. 2, ħω and ħk are expressed in Equations 4 and 5. If, εd=4, εm=-8 and εa=1 are applied in Equation 6, then sin θ= 0.53. Therefore, a resonance angle can be excited due to the -1<sin θ < 1. As a result, the conservation of energy (angular frequency, ħω) and momentum (ħk propagation) occurs [16]–[18]. Note: ω is the frequency of the incident light, c is the speed of light in vacuum, and εd and εa are the dielectric and metal permittivity, respectively.

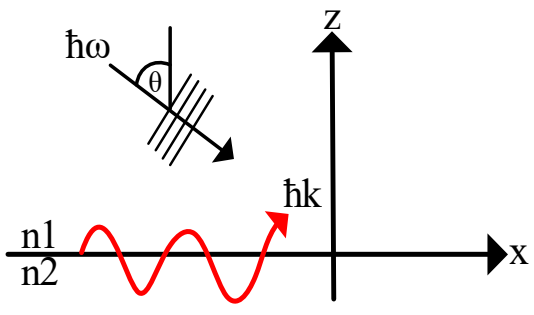

$$\hbar\omega = \frac{\omega}{c}\sqrt{\varepsilon d}\sin\theta \tag{4}$$

$$\hbar k = \frac{\omega}{c}\sqrt{\frac{\varepsilon m\cdot\varepsilon a}{\varepsilon m+\varepsilon a}} \tag{5}$$

$$\sin\theta = \sqrt{\frac{\varepsilon m}{\varepsilon d(\varepsilon m+1)}} \tag{6}$$

Fig. 2 *Wave vector propagation*

A non-coupling vector between a light line and a plasmonic wave concluded that a plasmonic wave could not be generated by any of the light rays [19], [20]. As shown in Fig. 3, the curve of the light line is not intercepted with any chosen metals such as gold (Au), silver (Ag), copper (Cu) and silicon dioxide (SiO2).

Int. Journal of Integrated Engineering Vol. 16 No. 7 (2024) p. 91-104

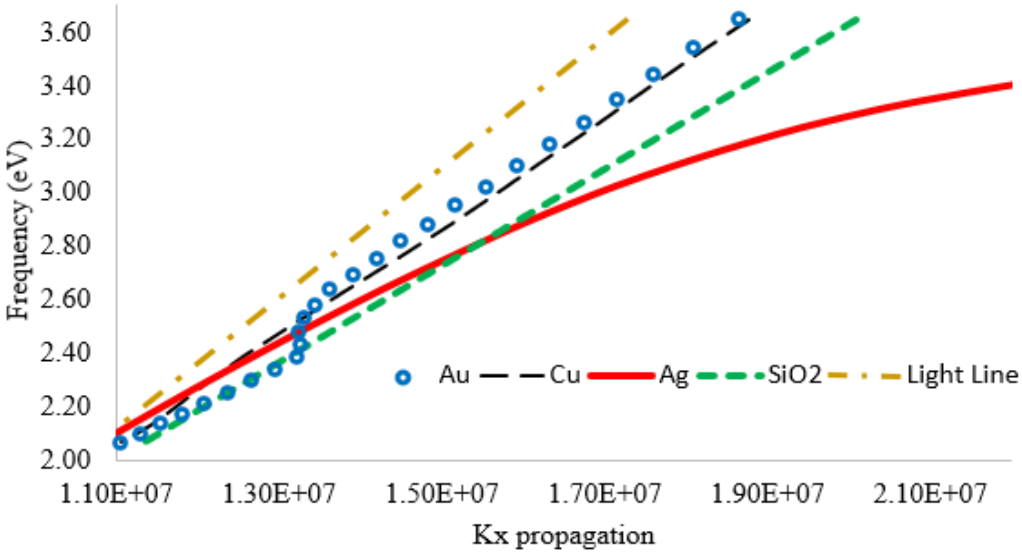

Fig. 3 *Dispersion for metals-air interfaces*

The intercept light line to the curve of the metal is necessary for plasmonic wave excitation. Given $\omega = ck_x/n_x$, the light line is dragged to cross the metal curves by increasing the vector of the evanescent' s refractive index (n_x) greater than one [21]. This is achieved via optical components such as prism, P-polarizer, diffraction grating and metals thickness lesser than 50 nm [22]. Eventually, the conservation of the energy ħω and momentum ħk vectors are successfully matched to generate the plasmonic wave for an effect of the resonance angle (θ_R) [23], [24]. By observing θ_R, the permittivity of the biological materials can be characterized as a function of dielectric properties at a great sensitivity and selectivity.

A therapeutic approach for cancer treatment was carried out via Photothermal therapy based on plasmonic gold nanoparticles (Au NP) [25]. A 532 nm laser excites 30 nm Au NP to generate localized heat on the U87MG malignant glioblastoma cells. Metabolic activity of cancer cells was decreased by a higher concentration of Au Np and laser power density at 92 µg/ mL and 96 mW/ cm2, respectively. However, laser absorption efficiency on the cancer cells was very low on the photothermal effects.

A novel biosensor configuration using plasmonic metal and photonic crystal was designed to detect basal cell cancer [26]. Silver/ Gallium arsenide, respectively were chosen as metal/insulators in two metal-insulator-metal (MIM) configurations to generate the Photonic Band Gap (PBG) transmission spectrum at 954nm to 2074 nm with sharp edges. The PBG behaves as an optical Biosensor, and Its transmission spectrum shifts to a higher wavelength when basal cells at different refractive indexes (r.i) are placed on the MIM surface. However, fabrication error and multi-mode spectra can cause inefficiency in light-plasmonic waveguide coupling and r.i interferences.

High spatial resolution was achieved for nanoparticle image reconstruction with Total Internal Reflection (TIR) via Surface Plasmon Resonance Microscopy (SPRM) [27]. A 720 nm laser, ½ wave plate, polarized beam splitter, lenses and tube lenses were used to produce P-polarized light to generate surface plasmon polariton mode for image captured via CMOS camera. Human IgG and goat-human IgG antibodies were applied in this experiment for Bio-molecule immobilization. The experiment concluded that nanoparticles and protein could amplify and enhance the measurement sensitivity with image resolution at 200 nm. However, the sensitivity of the TIR-SPRM technique becomes lower due to the shrinking image field and imaging algorithm.

Nanocomposite film revolutionizes potential applications in plasmonic biosensors with nanoparticle and matrix material [28]. A fiber biosensor probe was respectively modified and immobilized with nanocomposite film (gold nanoparticles, AuNPs/graphene oxide, GO) and anti-mouse IgG [29]. A tungsten halogen lamp is transmitted in a 2x1 fiber splitter to the fiber probe and reflected to the spectrometer. Higher sensitivity up to 79 nm/RIU was acquired with GO/ AuNPs fiber probe. However, a response from interfering antigens existed, slightly affecting the measurement selectivity.

Detection of uric acid (UA), xanthine (XA), and hypoxanthine (HXA) was expedited by the fabrication of a hybrid film with Metal-Organic Framework (MOF) based on Niobium (Nb) metal (Benzene 1,3,5-TriCarboxylic (BTC) acid)/ Nb(BTC)MOFs [30]. The hybrid film was synthesized via hydrothermal growth of NB(BTC)MOFs on the surface of CNFs. Differential Pulse Voltammetry (DPV) indicates electrochemical peaks at 272 mV (UA-XA) and 387 mV (XA-HXA) with significant differences within the range 0 ~ 1.0 V. However, diffusion-controlled electrooxidation slowed the reaction rate due to incomplete oxidation, electrode fouling and electrolyte depletion.

Optimizing plasmonic biosensors involves studying bending radii and temperature responses. The evanescent field allowed for U-shaped fiber resonant couplings with wavelength shifts [31]. To avoid surface imperfections, the standard telecom fiber (SMF-28e) polymer covering was cut in half and bent around the steel cylinder. The spectrum was measured using an LED (1.7 mW at 1550 nm) and an optical spectrum analyzer (Yokogawa AQ6375). The resonant shift shows refractive index variations from 1.33 to 1.37, suggesting a detection limit of 3.71×10-5. However, the thermo-optic impact dilatation on the metallic cylinder deteriorated with temperature.

Another progress was demonstrated by detecting water pathogens, urine, and serum via a plasmonic colorimetric Biosensor. A printed nanoarray had been fabricated and functionalized with antibodies to illuminate color upon pathogenic detection [32]. Linear response from 0 to 107 CFU mL^{-1} was achieved via colorimetric quantification with high selectivity, accuracy and sensitivity at 10 CFU mL-1. Due to variations in printing conditions, different qualities of printed nanoarrays have reduced the reproducibility, resolution, and accuracy.

A plasmonic biosensor based on refractive index (r.i.) was applied for malaria detection with infected red blood cells (IRBC). Black phosphor (BP) layers were coated in an orderly manner from bottom to top with BK7 prism, silver (Ag), BiFeO3, 2D nanomaterials, and IRBC [33]. Different Ag thicknesses from 40 nm, 45 nm, 50 nm, 55 nm, and 60 nm increase sensitivity (deg/RIU) to 224.28, 238.57, 251.42, 260, and 264.28, respectively. 2D nanomaterials with MXene, Graphene, and BP and found that they were sensitive at 218.57, 211.43, and 224.28 (deg/RIU). During the IRBC ring phase, the BP layer demonstrates a sensitivity of 461.43 deg/RIU. However, layers 1, 2, and 3 of the BP layers decrease sensitivity (deg/RIU) to 461.43, 218.57, and 185.71.

A Silicon-On-Insulator (SOI) photodiode (PD) with a gold (Au) antenna as a diffraction grating and gate electrode was demonstrated for refractive index (r.i) measurement [34]. Sucrose solutions at different concentrations were applied to evaluate PD's detection limit. A significant shift and peak were observed when the phase conditions of two diffracted lights at different wavelengths were matched. The wavelengths were modulated to the shorter wavelength and produced higher photocurrents when the Au antenna senses higher refractive index materials. However, signal drifts were observed in the measurement due to changes in r.i changed over the solution temperature. An SOI p–n junction diode-based temperature sensor with an isothermal response was used to reduce the signal drift.

Most of the works presented here did not discuss cost-effective, simplification and optimization parameters under the perspective of FEM and experimental works. Integration systems via photonics, electronics, and mechanical with software development should be discussed more. Theoretically and experimentally, past works should have discussed relationships more comprehensively. A lack of understanding in the FEM modelling complements the hardware development was explained. More is needed to know about the homemade system for generating and optimizing plasmonic waves. Rarely cost-effective approaches via 3D printing were used in the plasmonic biosensor. Even though many plasmonic biosensors exist in the market, the opto-plasmonic system will promote an alternative to a commercial solution. The objective is to perform cross-validation from Finite Element Modelling with an Opto-plasmonic system according to the Brewster, critical and resonance angles.

2. Methodology

2.1 Finite Element Modeling (FEM)

Wave Optics Module offers Electromagnetic Waves, Frequency Domain (EWFD) in Comsol Multiphysics software for finite element modeling (FEM) to solve time-harmonic electromagnetic field distributions [35]. As shown in Fig. 4(a), 2D geometries (Schott (N-BK7) – Gold (Au) – Air) were defined with frequency, lambda, theta1, theta2, refractive indexes (n1, n2), permittivity (ε1, ε2) at 461.5 THz, 650 nm, 30°, 48.6°, 2.25 and 1, respectively. The complex refractive index of the Au was referred from the Johnson & Christy database (n,k 0.188 μm -1.937 μm) [36]. A periodic condition to model the electromagnetic wave propagations was mapped for the above 2D homogenous geometries with the Floquet boundary condition. It allows periodicity structure in a k-vector to simulate the behavior of the electromagnetic dispersion in the frequency domain as expressed by the Floquet condition in Equation 7.

$$E_{dst} = E_{src} e^{-ikF(r_{dst} - r_{src})} \tag{7}$$

Note that k_F, *dst, src, E* and *r* are the Floquet wavenumber, destination variable, source variable, displacement field and spatial coordinates of the specified 2D boundary condition. As depicted in Figure 4(b), source (*src*) and destination (*dst*) boundaries are varied by a phase shift between the tangential components at equal symmetry and magnitude [35]. The phase shift relies on the Floquet wavenumber, source-destination distance and wave vector of incidence angle as expressed in Equation 8.

$$k_F = \{0, k_F\} = \{0, k_0 n_1 \sin\theta\} \tag{8}$$

Int. Journal of Integrated Engineering Vol. 16 No. 7 (2024) p. 91-104

The computational domain in Fig. 4(b) indicates that the Active port transmits the incident wave as a k-vector without any reflection to the Passive port at 1 W/m as input port power. Respectively, Active and Passive port wave excitation are set to ON and OFF. The source and destination boundaries were paired and meshed identically for better solution accuracy [35]. A range of parametric sweeps had been specified to obtain a response of the chosen variable when it gradually increases at specified intervals. The behavior of the build model for the electromagnetic distribution at different incidence angles is explored and analyzed. In this model, the parametric sweep for the k-vector is from 30° to 80° within 0.1° intervals at 474.7 THz.

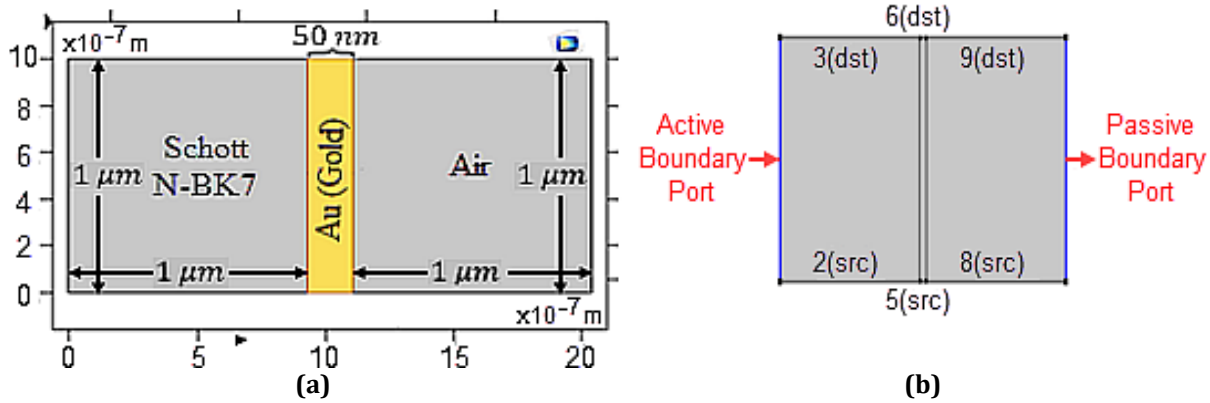

Fig. 4 *2D boundaries for (a) Prism-Au-Air interfaces; (b) Electromagnetic periodic condition*

2.2 Finite Element Modeling (FEM)

The Opto-plasmonic in Fig. 5 consists of two interfaces such as 1- Optical system (650 nm laser diode, laser driver, collimated lens, condenser lens, polarizer, prism and 50 nm gold (Au) layer) and 2- Electronic system (PC, microcontroller, photodiode, LCD, stepper driver and stepper motor).

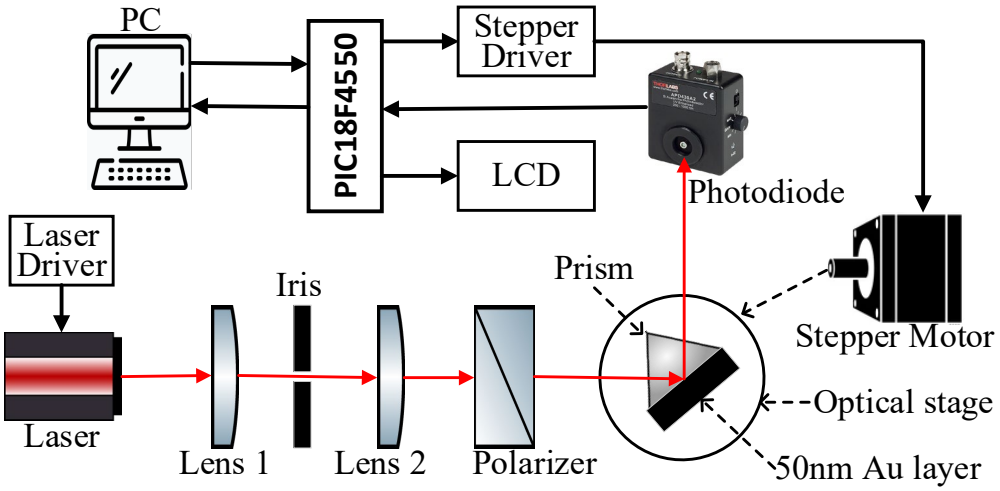

Fig. 5 *Opto-plasmonic system*

2.2.1 Optical System

Metals such as gold, silver, indium, aluminum, copper, platinum, titanium, chromium and others could generate plasmonic waves. However, gold (Au) is an inert substance and inoxidized, making it very stable as a perfect metal for biosensors. As shown in Fig. 6, gold was deposited on the prism using a DC magnetron sputtering to generate the plasmonic wave. The gold (Au) layer at 50 nm was deposited on the prism according to the recipe in Table 1 via a sputter coater. Sputtering time for different coating thicknesses can be determined according to Equation 9. Therefore, given x or coating thickness is 50 nm, y or sputter time will be approximately 68 seconds.

$$x = (0.6667 \times y) + 4.8889 \quad (9)$$

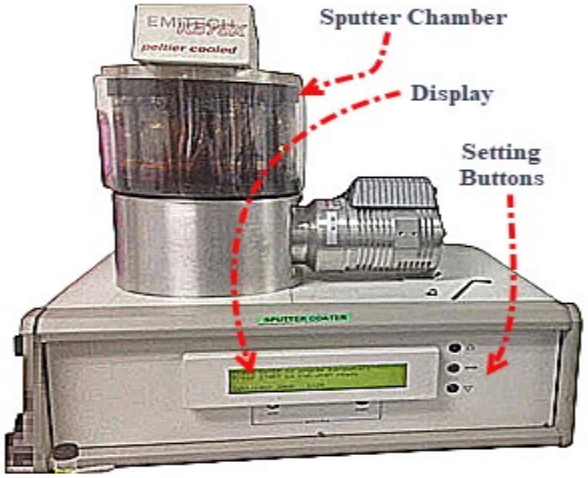

Fig. 6 *Sputter coater*

Table 1 *Coating parameters for Au layer*

Parameters	Value
Thickness	50 nm
Sputter time	68 sec
Argon gas pressure	5 psi
Clean current	105 mA
Sputtered current	20 mA

$$k_{x=}k_0\, n_{prism} \sin\theta_i \tag{10}$$

$$k_{pw=}k_0 \sqrt{\frac{\varepsilon_{metal}\varepsilon_{dielectric}}{\varepsilon_{metal}+\varepsilon_{dielectric}}} \tag{11}$$

Several considerations are necessary to fulfil an optics requirement for excitation of the plasmonic wave. As expressed in Equations 10 and 11, the N-BK7 prism at 1.5 refractive index must match the vector of light wave (k_x) and plasmonic wave (k_{pw}). When $k_x = k_{pw}$, the excitation of plasmonic waves is established to generate a plasmonic resonance. Wavelength beyond 500 nm showed unchanged energy distribution and perfect scattering, which led to 650 nm laser diode as a light source [10]. Unwanted diffraction is eliminated and the vertical slit or iris controls the resolution of the laser beam. Two collimated lenses were placed between the iris for correcting diverging beams due to misalignment of the reflected beams on the photodiode sensing pad. Plasmonic waves only exist in Transverse Magnetic mode or P-polarized. A mounted linear polarizer (LPVIS100, 550 nm ~ 1500 nm) was tuned to assure P-polarization transmission to the 50 nm gold-coated prism.

2.2.2 Electronic System

The electronics block diagram for the Opto-plasmonic system is visualized in Fig. 7 with two stepper motors plus a driver, prism, and photodiode. Referring to Fig. 8, they were retrofitted and mounted on the developed mechanical system. In equations 12 and 13, the stepper motor employed a micro-stepping for synchronizing photodiode/ prism stages to 3200/ 8000 steps at 0.1125°/ 0.045°, respectively.

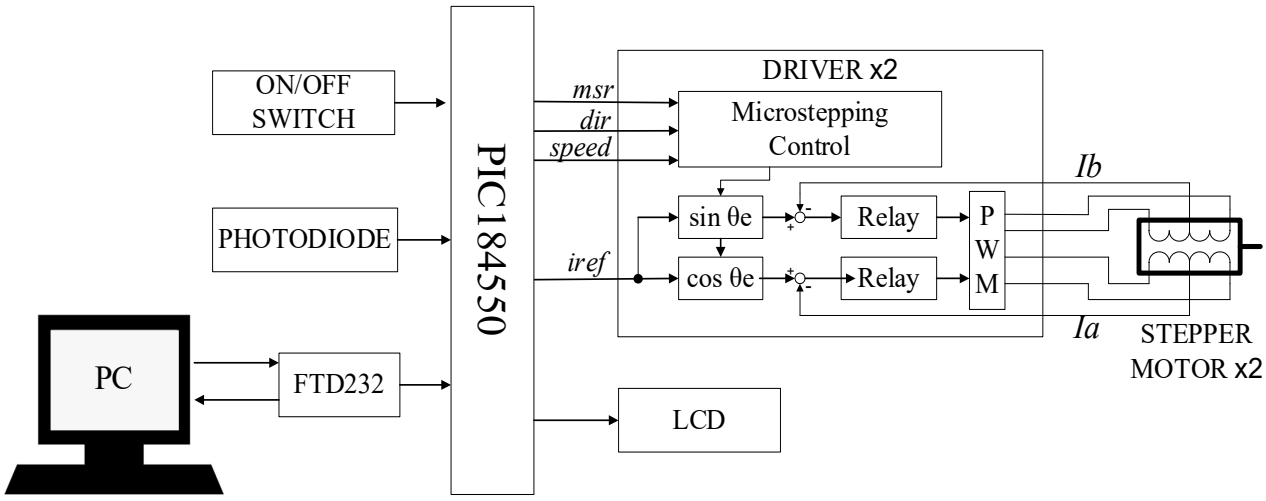

Fig. 7 *Electronics in Opto-plasmonic system*

$$I_a = I_0 \times \cos\theta_e \tag{12}$$

$$I_b = I_0 \times \sin\theta_e \tag{13}$$

Int. Journal of Integrated Engineering Vol. 16 No. 7 (2024) p. 91-104

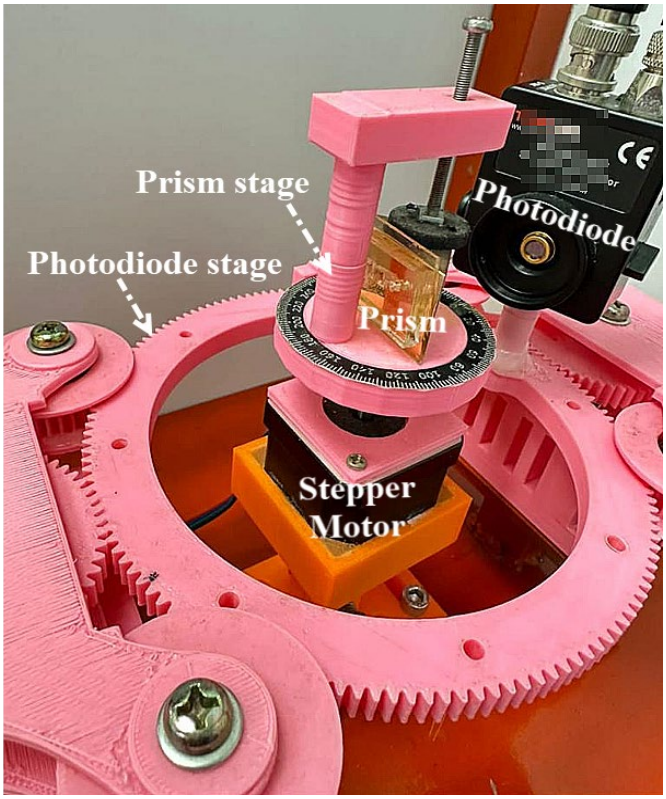

Fig. 8 *Mechanical system for Opto-plasmonic*

As the core processing unit, PIC184550 is equipped with an onboard programmable timer, 10-bit Analog Digital Converter (ADC), and Universal Synchronous Asynchronous Receiver Transmitter (USART). Timer, ADC and USART were used for 1- Generating pulse at 200 µs pulses, 2- Reading 10 bits ADC at 1.95 mV resolution/ 1.6 µs sampling rate and 3- Transmitting/ receiving serial communication data via PC at 19200 bps. The ADC results were averaged 50 times over to eliminate fluctuations due to 50 Hz interference. In opto-plasmonic, the microcontroller synchronizes two stepper motors and reads the reflectance beam via the fuzzy logic and photodiode [37]. As depicted in Fig. 9, the software was developed to perform controls such as Auto, Interval, Manual, Direction and Teach wiper.

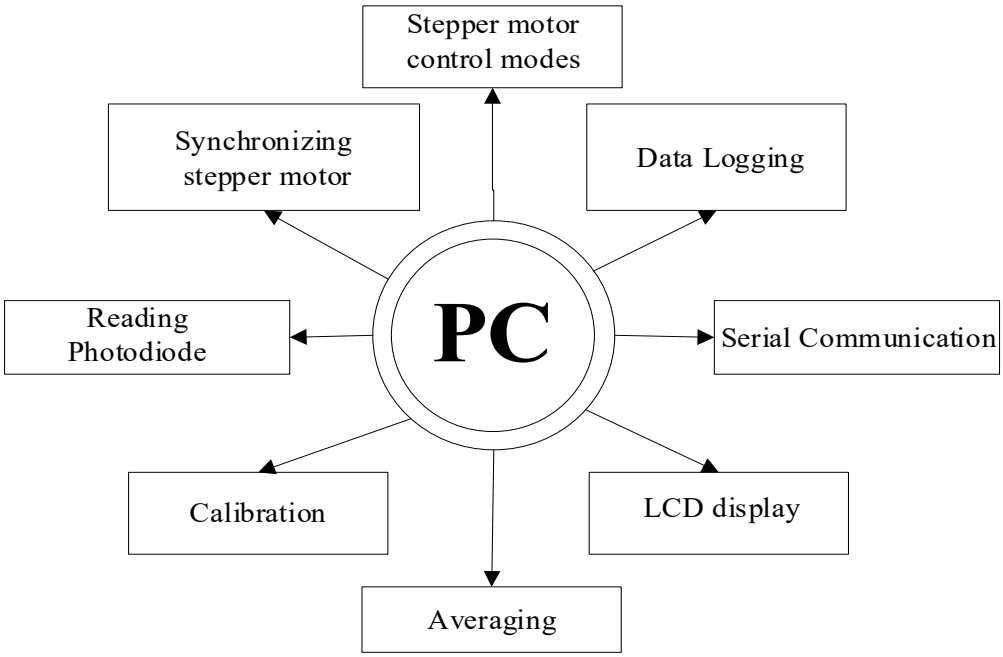

Fig. 9 *PC based system for Opto-plasmonic*

3. Result and Discussion

The plasmonic wave successfully modelled an electromagnetic distribution at different k-vectors from 30° to 80°. As shown in Fig. 10, 2D geometries from the left, middle and right regions are N-BK7 prism – Gold [Au] – Air. Note that right-side figures of Fig. 10 (a) ~ Fig. 10 (e) are zoomed-in sections from each left-side figure.

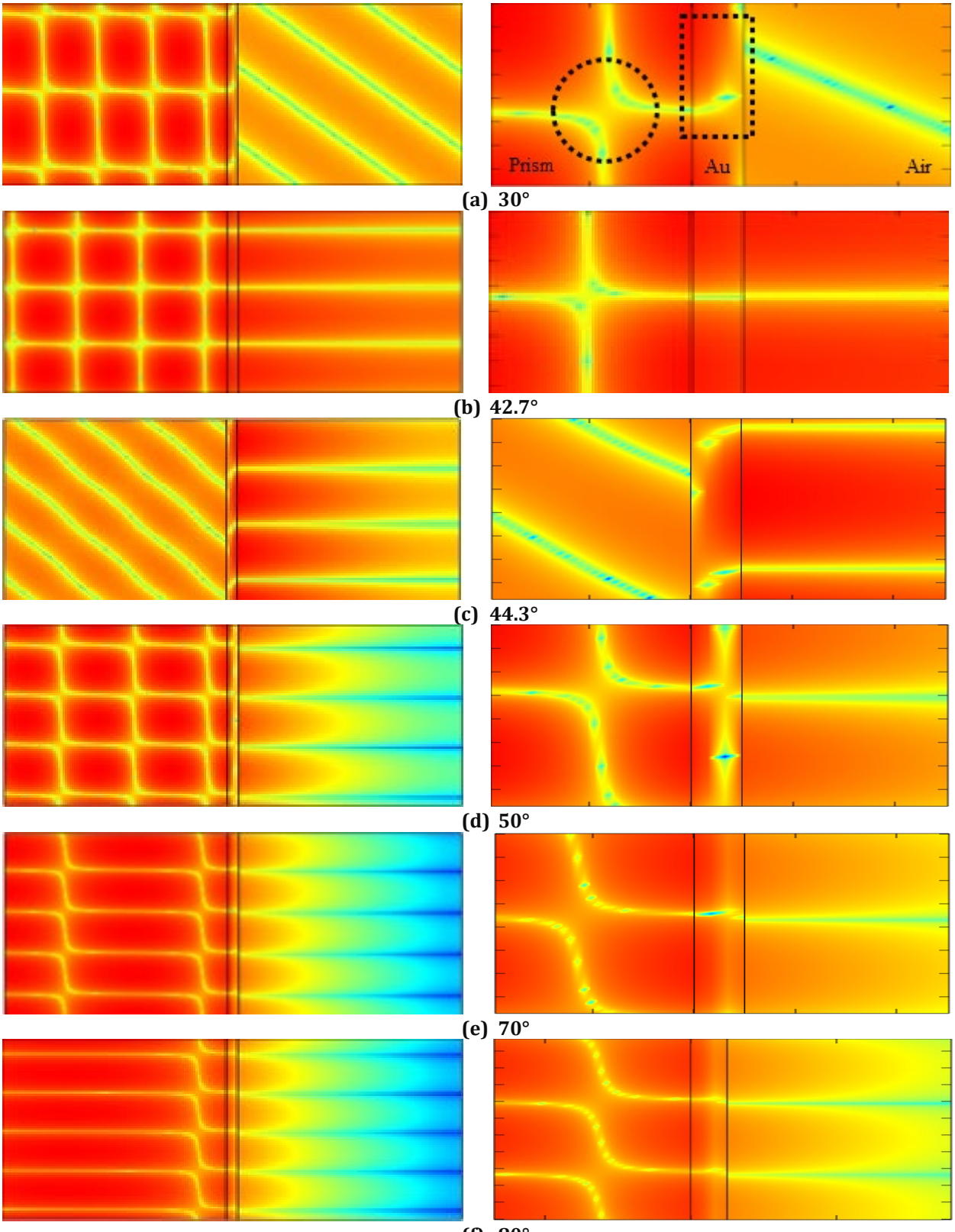

Fig. 10 *Electromagnetic distribution of plasmonic wave from 30° to 80°*

Int. Journal of Integrated Engineering Vol. 16 No. 7 (2024) p. 91-104

As shown in the dashed circle in Fig. 10(a), a wide energy gap was observed in the prism region as open contact in the gold (Au) region with diagonal refraction in the Air region. The plasmonic energy in Fig. 10(b) is initially generated at 42.7°, preferably known as a critical angle. A narrow energy gap is simulated and observed in the prism region. When the angle of incidence light is greater than a critical angle, a Total Internal Reflectance (TIR) will be performed. A zoom-in of Fig. 10(b) indicates that refraction of the critical angle is 90 degrees and observed as close contact in the gold (Au) region. This phenomenon reveals that a P-polarized light successfully penetrates through N-BK7 prism – Gold [Au] – Air mediums. Beyond the critical angle, the intensity gradually drops to a maximum attenuation at 44.3°. As shown in Fig. 11, this angle is known as a resonance angle and appears as a dark band that absorbs the reflected intensity due to the existence of the plasmonic energy. A zoom-in of Fig. 10(c) indicates that the narrow gap at critical is now widening and observed as open contact in the gold (Au) region. The energy gap keeps widening beyond the resonance angle, as shown in Fig. 10(c) to Fig. 10(f).

Fig. 11 *Plasmonics Resonance*

The reflectance of the plasmonic curve in Fig. 12 was plotted according to the finite element modeling. Due to the plasmonic wave excitation, equivalent critical/ resonance angles were plotted at 42.5°/ 44.3°, respectively.

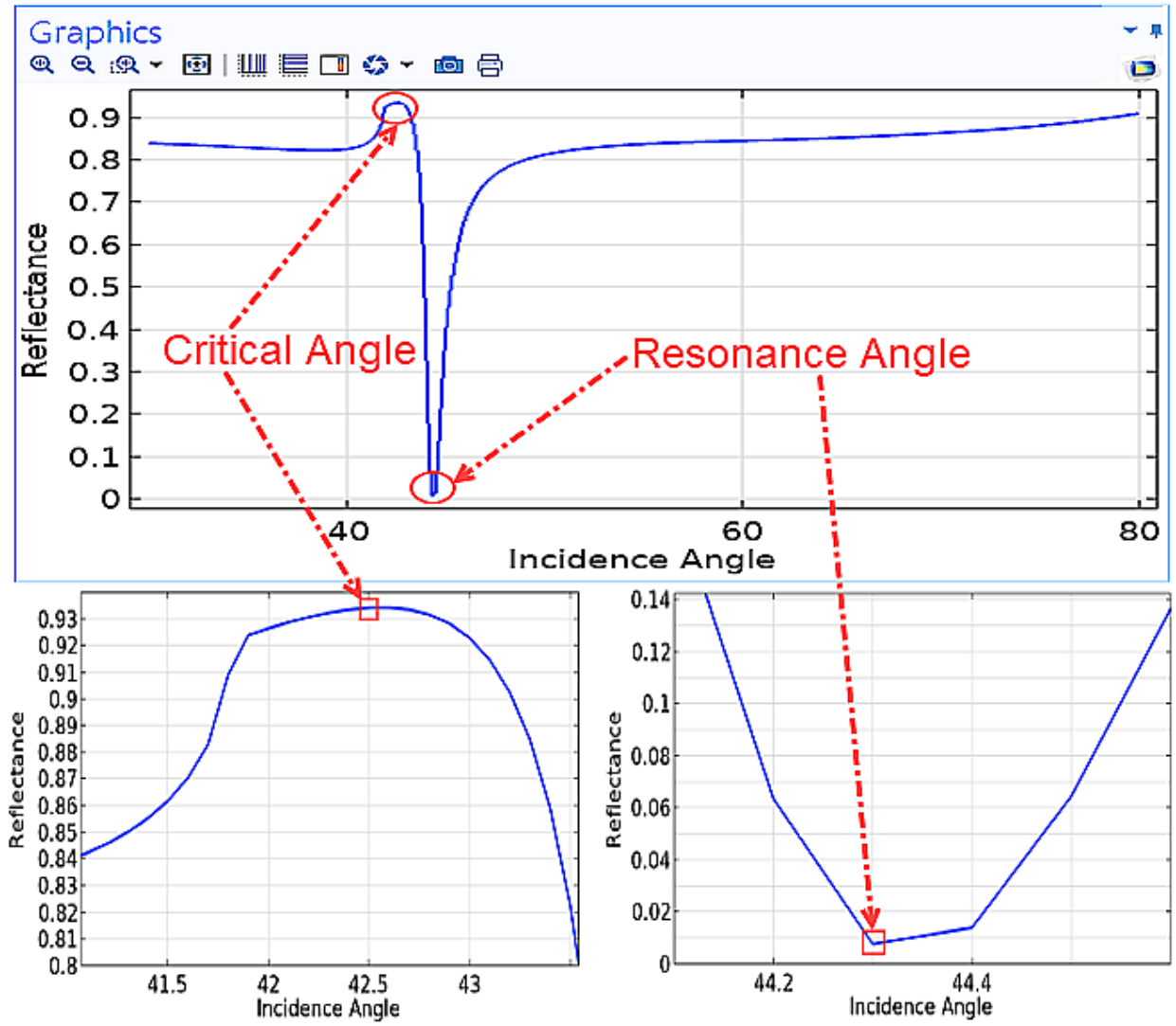

Fig. 12 *Reflectance of the plasmonic curve*

Fig. 13 indicates that two reflectivity curves were logged and plotted for the experiment with and without a 50 nm Au layer deposited on the prism. As shown in Fig. 13(a), intense plasmonic energy was generated with a sharp resonance dip at 45°/ 130° during the prism in pyramid/ inverse-pyramid positions, respectively. However, a dip at 130° was reserved as a system reference for mechanical calibration. On the contrary, no plasmonic energy could be generated in the Fig. 13(b). Neither a critical nor resonance angle could be observed due to the absence of a 50nm Au layer on the prism. No resonance will occur if the momentum (k-propagation) and energy conservation (angular frequency of incident light) are not matched.

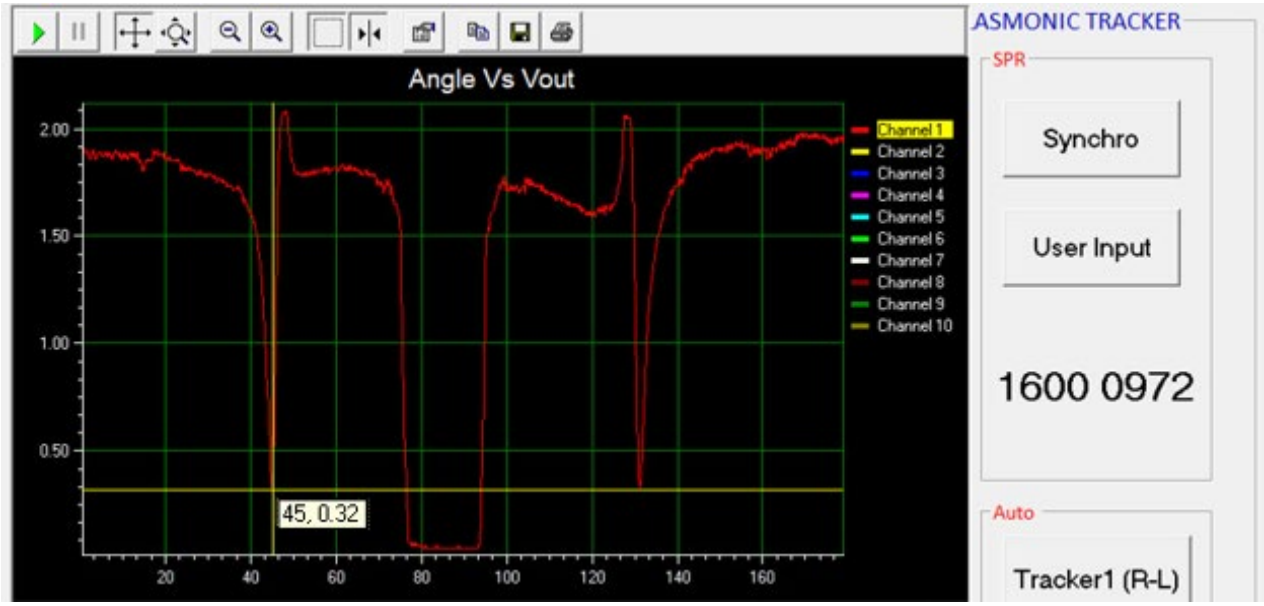

(a)

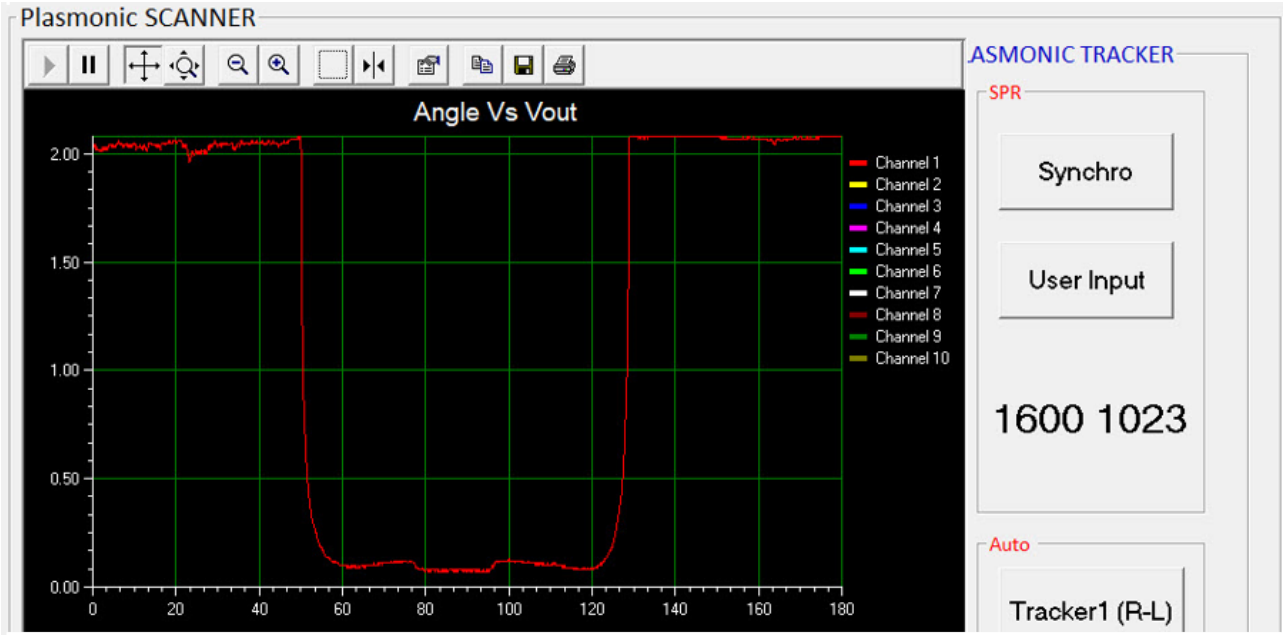

(b)

Fig. 13 *Reflectivity on (a) Plasmonic curve; (b) Non-plasmonic curve*

Since the plasmonic wave is under P-polarized mode, it is necessary to calibrate the optical system by tuning a linear polarizer according to the reflectivity. As shown in Fig. 14, the bare prism's reflectivity trace (dash line) was observed to confirm P-polarized transmission for a Brewster angle (θ_B). The reflectivity gradually decreases as the incidence angle (θi) increases. θ_B is observed when the reflectivity hits zero reflectance. Beyond the θ_B, the reflectivity gradually increases and this verified the P-polarized light wave. The reflectivity will keep increasing until it hits a critical angle at θ_{C1}. Beyond this angle, the reflectance becomes saturated. Therefore, Total Internal Reflection (TIR) is achieved when $\theta i > \theta_{C1}$.

Int. Journal of Integrated Engineering Vol. 16 No. 7 (2024) p. 91-104

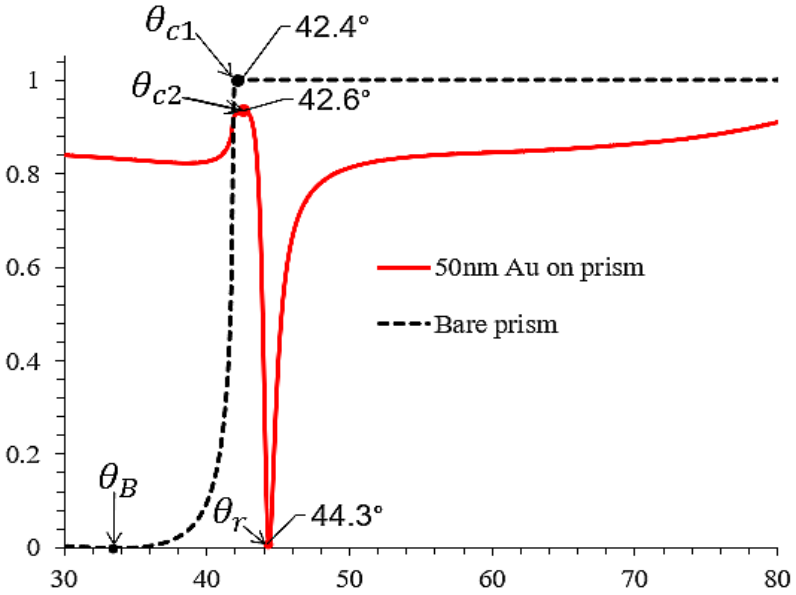

Fig. 14 *P-polarized mode according to Brewster's angle (θ_B)*

The plotted plasmonic curve in Fig. 15 was acquired from experiment (Exp) and compared with the finite element modeling (FEM). The results satisfy each other, especially on the accuracy of both resonance angles.

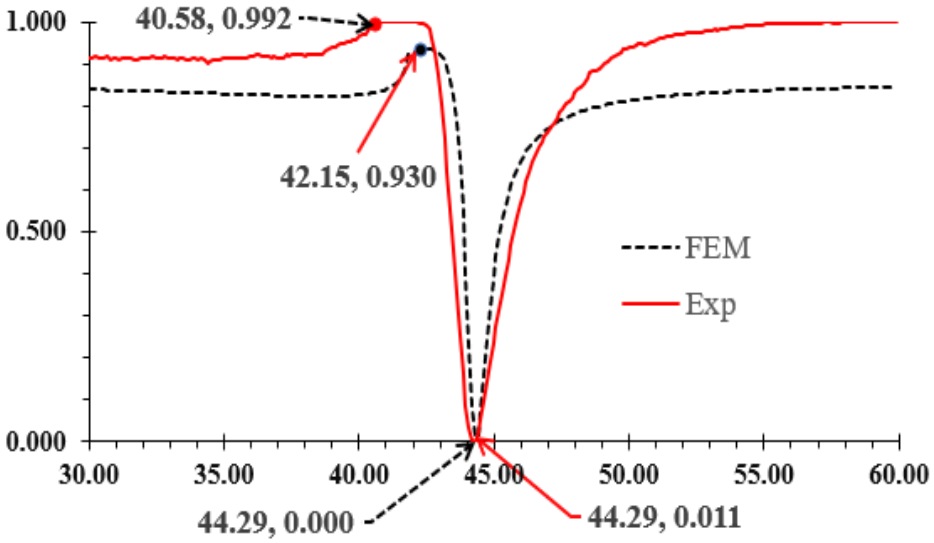

Fig. 15 *Plasmonic curves via FEM and Opto-plasmonic experiment*

Further comparisons in Fig. 16 on different qualitative parameters are summarized in Table 2. The experiment result via the Opto- plasmonic to FEM indicates percentage differences for Θc, Θr, Δr, FWHM, and Rmin at 3.72%, 0.2%, 3.37%, 4.64% and 0%, respectively. As a result, excellence validation was successfully achieved between FEM and Opto- plasmonic.

Table 2 *FEM Vs. experiment parameters*

Parameters	FEM	EXP	Δ%
Critical Angle, θc	42.15	40.58	-3.72
Resonance Angle, θr	44.5158	44.60431	0.20
Curve Depth, Δr	0.89	0.92	3.37
Full Width Half Maximum, FWHM	1.206	1.262	4.64
Minimum Reflectance, Rmin	0.001	0.001	0

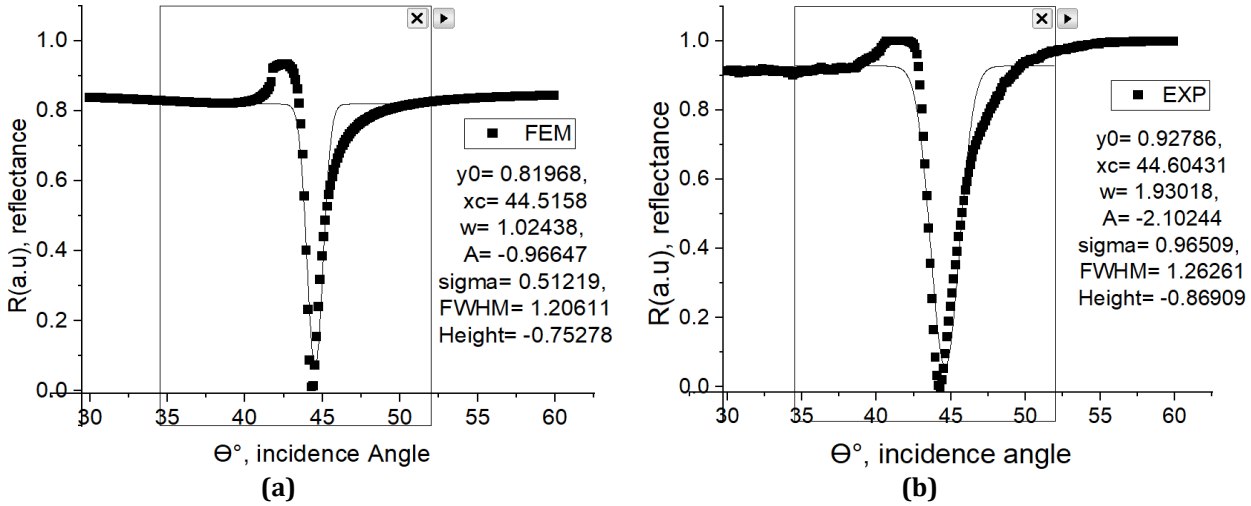

Fig. 16 *Comparison of the (a) Finite element modeling (FEM); (b) Experiment via Opto-plasmonic*

4. Conclusion

The plasmonic wave was simulated and validated via finite element modeling (FEM) and Opto-plasmonic system. Both bare/ coated prisms indicate total internal reflection (TIR) with a critical angle (42°). However, only a prism deposited with a 50 nm Au layer could generate the plasmonic wave with a resonance angle (44.3°). A slight percentage difference on Θc, Θr, Δr, FWHM, and Rmin indicates excellence validation between FEM and Opto-plasmonic. However, improvements can be made to portability and system optimization. In future, the Opto-plasmonic will be miniaturized and optimized via integration with nanocomposite materials such as graphene, carbon nanotube, quantum dots, nanoparticles and polymer.

Acknowledgement

This study was funded by the Malaysia Ministry of Higher Education through the Fundamental Research Grant Scheme (FRGS) FRGS/1/2020STK0/UNIKL/02/5 and supported by Nutrition, Metabolic & Cardiovascular Research Centre (NMCRC), Institute for Medical Research, Ministry of Health Malaysia.

Conflict of Interest

Authors declare that there is no conflict of interests regarding the publication of the paper.

Author Contribution

The authors confirm contribution to the paper as follows: ***study conception and design:*** *Muhammad Rosli Abdullah, Noor Hasmiza Harun;* ***data collection:*** *Muhammad Rosli Abdullah, S Noorjannah Ibrahim, Azimah Abdul Wahab, Mohd Azerulazree Jamilan;* ***analysis and interpretation of results:*** *Muhammad Rosli Abdullah, Noor Hasmiza Harun;* ***draft manuscript preparation:*** *All authors. All authors reviewed the results and approved the final version of the manuscript.*

References

[1] S. Kumar and S. Seo, "Plasmonic Sensors: A New Frontier in Nanotechnology," *Biosensors (Basel)*, vol. 13, no. 3, 2023. https://doi.org/10.3390/bios13030385

[2] W. Jiang *et al.*, "Active Site Engineering on Plasmonic Nanostructures for Efficient Photocatalysis," *ACS Nano*, vol. 17, no. 5, pp. 4193–4229, Mar. 2023, https://doi.org/10.1021/acsnano.2c12314

[3] E. Ferrari, "Gold Nanoparticle-Based Plasmonic Biosensors," *Biosensors*, vol. 13, no. 3. MDPI, Mar. 01, 2023. https://doi.org/10.3390/bios13030411

[4] F. Kurul, Z. A. Yazici, Z. A. Kocer, S. N. Topkaya, and A. E. Cetin, "Low-cost and portable plasmonic biosensor for label-free detection of viruses in resource-limited settings," in *Proc.SPIE*, Aug. 2023, p. 126272O. https://doi.org/10.1117/12.2671001.

[5] A. K. Mishra *et al.*, "Plasmonic Solar Energy Harvesting by ZnO Nanostructures and Their Composite Interfaces: A Review on Fundamentals, Recent Advances, and Applications," *Energy Technology*, vol. 11, no. 7, p. 2201393, Jul. 2023. https://doi.org/10.1002/ente.202201393.

[6] Y. Xi *et al.*, "Plasmonic Resonance Enabling 2D Perovskite Single Crystal to Detect Telecommunication Light," *Adv Opt Mater*, vol. 11, no. 6, p. 2202423, Mar. 2023. https://doi.org/10.1002/adom.202202423
[7] C. Caucheteur and Médéric Loyez, *Plasmonic Optical Fibre Biosensors*. Artech House, 2023. https://us.artechhouse.com/Plasmonic-Optical-Fiber-Biosensors-P2331.aspx
[8] A. Shaaban and Y.-C. Du, "An Optical Universal Plasmon-Based Biosensor for Virus Detection," *J Med Biol Eng*, vol. 43, no. 3, pp. 258–265, 2023. https://link.springer.com/article/10.1007/s40846-023-00788-x
[9] M. Khodadadi, S. M. M. Moshiri, N. Nozhat, and M. Khalily, "Controllable hybrid plasmonic integrated circuit," *Sci Rep*, vol. 13, no. 1, p. 9983, 2023. https://www.nature.com/articles/s41598-023-37228-4
[10] M. Abdullah and N. Harun, *Preliminary study in microfluidic channel and gold nanoparticles with finite element simulation on biosensor development*, vol. 2129. 2019. https://doi.org/10.1063/1.5118130
[11] J. Zhang, A.-D. Liu, C. Li, and C. Zhang, "Extended Snell's law based on surface current radiation," *J. Opt. Soc. Am. B*, vol. 39, no. 7, pp. 1919–1925, Jul. 2022. https://opg.optica.org/josab/abstract.cfm?uri=josab-39-7-1919
[12] F. J. Kadhum, S. A. Mohammed, J. S. Alikan, S. H. Kafi, A. A. Al-Zuky, and A. H. Al-Saleh, "Silver Prism Interface Plasmon Resonance for Biosensor in IR-Visible Spectrum Region," in *Materials Science Forum*, Trans Tech Publications Ltd, 2023, pp. 39–50. https://www.scientific.net/MSF.1083.39
[13] N. Navaratna, Y. J. Tan, A. Kumar, M. Gupta, and R. Singh, "On-chip topological THz biosensors," *Appl Phys Lett*, vol. 123, no. 3, p. 033705, Jul. 2023. https://doi.org/10.1063/5.0157357
[14] R. P. Potdar, Y. B. Khollam, S. F. Shaikh, R. W. Raut, B. Pandit, and P. S. More, "Evanescent wave sensor for potassium ion detection with special reference to agricultural application," *J Photochem Photobiol A Chem*, vol. 441, p. 114707, 2023. https://doi.org/10.1016/j.jphotochem.2023.114707
[15] X. Chen and M. Andrews, "Integrated Optics Polarized Light and Evanescent Wave Surface-Enhanced Raman Scattering to detect ligand Interactions at nanoparticle surfaces," *ChemRxiv*, 2023. https://chemrxiv.org/engage/chemrxiv/article-details/645db842f2112b41e9696fe4
[16] H. Zhang, M. Ijaz, and R. J. Blaikie, "Recent review of surface plasmons and plasmonic hot electron effects in metallic nanostructures," *Front Phys (Beijing)*, vol. 18, no. 6, p. 63602, 2023. https://link.springer.com/article/10.1007/s11467-023-1328-9
[17] Gupta, D. Banshi, Sharma, K. Anuj, Li, and Jin, *Plasmonics-Based Optical Sensors and Detectors*. CRC Press, 2023. https://doi.org/10.1201/9781003438304
[18] Y. Xu, M. Sun, H. Wu, Y. Song, and Q. Wang, "Plasmonic Biosensor Based on Ag-TiO2-ZnO Gratings for Cancer Detection in the Optical Communication Band," *IEEE Sens J*, p. 1, 2023. https://ieeexplore.ieee.org/document/10213422
[19] C. Kar, S. Jena, D. V Udupa, and K. D. Rao, "Tamm plasmon polariton in planar structures: A brief overview and applications," *Opt Laser Technol*, vol. 159, p. 108928, 2023. https://doi.org/10.1016/j.optlastec.2022.108928
[20] S. Juodkazis and S. H. Ng, "Nanoscale Plasmonic Printing Laser Printing of Nanophotonic Structures View project Nanostructures for Highly Efficient Infrared Detection View project Nanoscale plasmonic printing," 2022. https://www.preprints.org/manuscript/202202.0258/v1
[21] A. Zahra, M. Abbas, and R. Ullah, "Amplification and Excitation of Surface Plasmon Polaritons via Four-Wave Mixing Process," Aug. 2023, [Online]. Available: http://arxiv.org/abs/2308.11899
[22] S. Akgönüllü and A. Denizli, "Plasmonic nanosensors for pharmaceutical and biomedical analysis," *J Pharm Biomed Anal*, p. 115671, 2023. https://doi.org/10.1016/j.jpba.2023.115671
[23] M. Li, S. Yan, Y. Zhang, Y. Zhou, and B. Yao, "Orbital angular momentum in optical manipulations," *Journal of Optics*, vol. 24, no. 11, p. 114001, 2022. https://iopscience.iop.org/article/10.1088/2040-8986/ac9192
[24] Z. Hayran, J. B. Khurgin, and F. Monticone, "$\hbar\omega$ versus $\hbar$k: dispersion and energy constraints on time-varying photonic materials and time crystals [Invited]," *Opt Mater Express*, vol. 12, no. 10, p. 3904, Oct. 2022. https://doi.org/10.1364/OME.471672
[25] B. K. Jalali, S. S. Shik, L. Karimzadeh–Bardeei, E. Heydari, and M. H. M. Ara, "Photothermal treatment of glioblastoma cells based on plasmonic nanoparticles," *Lasers Med Sci*, vol. 38, no. 1, p. 122, 2023. https://link.springer.com/article/10.1007/s10103-023-03783-5
[26] S. Khani and M. Hayati, "Optical biosensors using plasmonic and photonic crystal band-gap structures for the detection of basal cell cancer," *Sci Rep*, vol. 12, no. 1, p. 5246, 2022. https://www.nature.com/articles/s41598-022-09213-w
[27] T. Zhang *et al.*, "Surface Plasmon Resonance Microscopy Based on Total Internal Reflection," *Biosensors (Basel)*, vol. 13, no. 2, 2023. https://doi.org/10.3390/bios13020261
[28] A. A. Al-Muntaser *et al.*, "Boosting the optical, structural, electrical, and dielectric properties of polystyrene using a hybrid GNP/Cu nanofiller: novel nanocomposites for energy storage applications," *Journal of Materials Science: Materials in Electronics*, vol. 34, no. 7, p. 678, 2023. https://link.springer.com/article/10.1007/s10854-023-10104-7

[29] H. T. Chou, Y. Sen Liao, T. M. Wu, S. H. Wang, K. H. Chiang, and W. C. Su, "Development of Localized Surface Plasmon Resonance-Based Optical Fibre Biosensor for Immunoassay Using Gold Nanoparticles and Graphene Oxide Nanocomposite Film," *IEEE Sens J*, vol. 22, no. 7, pp. 6593–6600, Apr. 2022. https://ieeexplore.ieee.org/document/9698179
[30] B. Dey, Md. W. Ahmad, G. Sarkhel, G. Ho Lee, and A. Choudhury, "Fabrication of niobium metal organic frameworks anchored carbon nanofibre hybrid film for simultaneous detection of xanthine, hypoxanthine and uric acid," *Microchemical Journal*, vol. 186, p. 108295, 2023. https://doi.org/10.1016/j.microc.2022.108295
[31] Carolina Londero, Martina Delgado-Pinar, Christian Cuadrado-L, and Miguel V. Andrésaborde, "Resonant couplings in U-shaped fibres for biosensing," *Journal of Lightwave Technology* , pp. 1–8, Mar. 2023. https://ieeexplore.ieee.org/document/10080961
[32] Z. Zhang *et al.*, "Rapid Identification and Monitoring of Multiple Bacterial Infections Using Printed Nanoarrays," *Advanced Materials*, vol. 35, no. 12, p. 2211363, Mar. 2023. https://doi.org/10.1002/adma.202211363
[33] M. G. Daher, Y. Trabelsi, Y. K. Prajapati, A. Panda, N. M. Ahmed, and A. N. Z. Rashed, "Highly sensitive detection of infected red blood cells (IRBCs) with plasmodium falciparum using surface plasmon resonance (SPR) nanostructure," *Opt Quantum Electron*, vol. 55, no. 3, Mar. 2023. https://link.springer.com/article/10.1007/s11082-022-04466-1
[34] H. Satoh *et al.*, "Refractive Index Measurement Using SOI Photodiode with SP Antenna toward SOI CMOS-Compatible Integrated Optical Biosensor," *Sensors*, vol. 23, no. 2, 2023. https://doi.org/10.3390/s23020568
[35] "WaveOpticsModuleUsersGuide." https://doc.comsol.com/5.4/doc/com.comsol.help.woptics/WaveOpticsModuleUsersGuide.pdf (accessed May 08, 2023).
[36] "Refractive index of Au (Gold) - Johnson." https://refractiveindex.info/?shelf=main&book=Au&page=Johnson (accessed May 01, 2023).
[37] M. R. Abdullah, N. H. Harun, and R. A. A. Raof, "Microstepping synchronization via hybridization of Mamdani's Fuzzy Logic for the plasmonic tracker," in *Journal of Physics: Conference Series*, IOP Publishing Ltd, Aug. 2021. https://iopscience.iop.org/article/10.1088/1742-6596/1997/1/012033